Original Article

CCL2-FUNCTIONALIZED COMPOSITE SCAFFOLDS ENHANCE BONE REGENERATION VIA SYNERGY OF OSTEOGENESIS AND ANGIOGENESIS

Zhen Liang[1,2,§], Xin Peng[3,§], He Pang[2], Haina Yang[4], Bin Xie[2], Chengshuo Huang[1,2], Zhanpeng Su[2], Bo Wei[1,2,*] and Sien Lin[1,2,5,*]

[1]Dr. Neher's Biophysics Laboratory for Innovative Drug Discovery, State Key Laboratory of Quality Research in Chinese Medicine, Macau University of Science and Technology, Macau, China
[2]Department of Minimally Invasive Spine Surgery, Affiliated Hospital of Guangdong Medical University, 524001 Zhanjiang, Guangdong, China
[3]Department of Orthopedics, Dongshan Hospital, 514000 Meizhou, Guangdong, China
[4]Department of Obstetrics and Gynecology, Affiliated Hospital of Guangdong Medical University, 524001 Zhanjiang, Guangdong, China
[5]Department of Orthopaedics and Traumatology, School of Clinical Medicine, Li Ka Shing Faculty of Medicine, The University of Hong Kong, Hong Kong SAR, China
[§]These authors contributed equally.

Abstract

Background: Chemokine (C-C motif) ligand 2 (CCL2) enhances bone regeneration when integrated into a composite scaffold and show promise for clinical applications in persistent bone defects. **Methods:** A composite biodegradable scaffold was fabricated using 3D bioprinting with a polylactic acid-glycolic acid copolymer (PLGA) and β-tricalcium phosphate (β-TCP). Gelatin methacrylate (GelMA) hydrogel was used as carrier of CCL2 to enable prolonged release. The scaffolds were immersed in GelMA solution with or without CCL2. *In vitro* experiments were conducted to analyze the kinetics of CCL2 release and its influence on the proliferation and osteogenic differentiation of rat bone marrow mesenchymal stem cells (BMSC). Scaffolds PLGA/β-TCP (PT), GelMA/PLGA/β-TCP (GPT), and CCL2-conjugated GelMA/PLGA/β-TCP (CGPT) were implanted into a rat femoral defect model (n = 8) and analyzed to evaluate bone mass regeneration at 4 and 8 weeks. **Results:** CGPT exhibited a prolonged release period lasting 30 days. *In vitro*, CCL2 significantly promoted BMSCs proliferation ($p < 0.05$) and the formation of mineralized nodules, and it markedly increased tube formation in HUVECs. In the femoral defect model, bone mineral density and volume fraction in the CGPT group increased compared to the controls (PT, GPT, and control) after implantation. Histological analysis revealed enhanced new bone formation, and integration of the scaffold with surrounding tissue in this group. The expression of osteogenic markers (runt-related transcription factor 2 (Runx2), osteocalcin (OCN), and osteopontin (OPN)) and the angiogenic factor vascular endothelial growth factor (VEGF) significantly increased at the defect site within the CGPT group. **Conclusions:** Scaffolds made from a composite of GelMA-infused 3D-printed PLGA/β-TCP incorporated with CCL2 greatly enhance osteogenesis and angiogenesis to facilitate bone healing.

Keywords: CCL2, composite scaffolds, bone repair, bone Defects, cytokines.

***Address for correspondence**: Bo Wei, Dr. Neher's Biophysics Laboratory for Innovative Drug Discovery, State Key Laboratory of Quality Research in Chinese Medicine, Macau University of Science and Technology, Macau, China; Department of Minimally Invasive Spine Surgery, Affiliated Hospital of Guangdong Medical University, 524001 Zhanjiang, Guangdong, China. E-mail: web-jxmc@163.com; Sien Lin, Dr. Neher's Biophysics Laboratory for Innovative Drug Discovery, State Key Laboratory of Quality Research in Chinese Medicine, Macau University of Science and Technology, Macau, China; Department of Minimally Invasive Spine Surgery, Affiliated Hospital of Guangdong Medical University, 524001 Zhanjiang, Guangdong, China; Department of Orthopaedics and Traumatology, School of Clinical Medicine, Li Ka Shing Faculty of Medicine, The University of Hong Kong, Hong Kong SAR, PR China. E-mail: sienlin@hku.hk.

Introduction

The occurrence of delayed healing and non-union in bones poses a considerable obstacle in orthopedic care, significantly affecting the well-being of patients [1]. This issue arises from multiple factors, including chronic infections, aggressive conditions like bone tumors, fractures that involve severe soft tissue damage (e.g., multiple open fractures), and individual patient characteristics, including older age, comorbidities, and weakened immune systems [2]. Presently, targeted treatment options include autologous or allogeneic bone grafts, vascularized fibula grafting, and the Masquelet technique, among others [3,4]. Bone grafting, a practice that has been in use for over a century [5], continues to be the most common method for treating bone defects, typically provoking a low immune response[6]. However, autologous grafting has its limitations, such as donor site pain and restricted availability, which can heighten the risk of infection due to surgical trauma [7]. In contrast, allogeneic grafting is gaining traction in clinical practice because of its greater availability and adaptability in size, although it carries the potential for immunogenic reactions and disease transmission [8]. Therefore, our aim is to create a safe and effective biomaterial that promotes bone regeneration and accelerates healing.

Chemokine (C-C motif) ligand 2 (CCL2), also referred to as monocyte chemokine 1 (MCP1) [9], is recognized as the first CC chemokine identified in humans. Found on chromosome 17, CCL2 consists of 76 amino acids and has a molecular weight of 13 kDa. It can be produced and released by a variety of cells, such as epithelial, endothelial, smooth muscle cells, fibroblasts, and monocytes. CCL2 plays a vital role in directing the movement and infiltration of monocytes and macrophages [10,11]. Research by Whelan DS and colleagues suggested that CCL2 derived from mesenchymal stem cells (MSCs) enhances the effectiveness of MSC therapy by facilitating the repolarization of macrophages [12], a crucial step for wound healing induced by MSCs, which is also important for the regeneration of articular cartilage [13]. Consequently, CCL2 may be essential in the inflammatory response of hematomas during the initial stages of fracture healing. In the realm of bone repair, angiogenesis and bone remodeling are closely linked processes. A significant factor affecting fracture healing is the degree of blood supply disruption at the injury site. The role of CCL2 in angiogenesis is notable, as the CCL2/CCR2 signaling pathway greatly enhances this process [14]. CCL2 functions as a regulatory element in angiogenesis by activating the ETS-1 transcription factor in vascular endothelial cells [15] and indirectly fostering angiogenesis through the modulation of mononuclear macrophages [12,16–18]. Additionally, CCL2 has been implicated in bone healing by coordinating inflammatory responses with bone remodeling, thereby facilitating effective skeletal repair [19,20]. It mediates mechanical responses between osteoblasts and bone mesenchymal cells [21] and is crucial for the formation of osteoclasts[22]. Moreover, CCL2 influences the recruitment of macrophages and osteoclasts, thereby promoting the growth of prostate tumors and their metastasis to bone [23]. Importantly, CCL2 shows the highest levels of induction of parathyroid hormone (PTH) during intermittent therapy [9], working in conjunction with PTH to affect bone dynamics. PTH activates the PKA pathway in osteoblasts, which increases the expression and release of CCL2, further encouraging the recruitment of osteoclasts and their precursor monocytes for bone remodeling [24]. Thus, strategies to harness CCL2 are of great importance. Presently, 3D printing has gained traction as a method for creating composite scaffolds [25,26]. This technology allows for the fabrication of biocompatible scaffolds that incorporate bioactive factors or specific medications, customized to fit the shape of bone defects in patients with particular lesions, while also mimicking the pore structures and mechanical characteristics of natural bone. Various materials have been utilized in bone tissue engineering, with polylactic acid-glycolic acid copolymer (PLGA) being a prominent synthetic polymer known for its simple production and cost-effectiveness, making it suitable for large-scale applications. Its high biocompatibility and controllable degradation rates, comparable to those of natural polymers, position PLGA as an ideal carrier [27]. β-tricalcium phosphate (β-TCP), an inorganic material, is noted for its excellent mechanical properties and significant osteoinductive potential, playing a key role in bone mineralization [28]. It is employed as a delivery system for various bioactive factors, including bone morphogenetic protein (BMP2) and VEGF [29,30].

This study posits that CCL2 is crucial for angiogenesis and aids in the healing of bones. We developed an innovative composite scaffold by integrating CCL2 with a PLGA/β-TCP scaffold, which was then immersed into a 10% GelMA hydrogel solution. The influence of CCL2 on bone development and blood vessel formation was examined through both a cellular model and an *in vivo* study involving femoral defects in rats.

Materials and Methods

Animals and Ethics Approval

This study employed 32 male rats, each 12 weeks old and weighing approximately 400 grams (with a variance of $\pm$ 30 g). The subjects were descendants of rats procured from Sperfu (Beijing) Biotechnology Co., Ltd., and were kept in typical laboratory settings. The Laboratory Animal Ethics Committee of Guangdong Medical University granted approval for all experimental activities (Approval ID: GDY1902126; Date: May 25, 2019). All pertinent guidelines and regulations were adhered to throughout the study, ensuring that anesthesia and euthanasia were carried out in strict accordance with the ARRIVE guidelines. Sodium pentobarbital at a 1% concentration was the chemical used in the animal experiments.

Preparation of Composite Porous Material Scaffolds

A solution consisting of 8% (W/V) PLGA (RESOMER; Boehringer-Ingelheim, Germany) and 2% (W/V) β-TCP [31,32] (Sigma-Aldrich, Germany) was mixed to create a consistent liquid paste, which was subsequently printed via a 3D bioprinter (CLRF-2000-II; Tsinghua University, China). This process yielded a PLGA/β-TCP composite porous scaffold, as referenced in our previous study [32]. A 10% GelMA hydrogel solution (EFL-GM60; Suzhou Yongqinquan Intelligent Equipment Co., Ltd., China) was prepared and subjected to ultrasound until fully dissolved. A scaffold block of 5 × 5 × 5 mm was immersed into this solution. A 1-mL syringe needle was inserted into the center of the block, and through repeated suction, the GelMA hydrogel permeates the material's pores. The GelMA hydrogel/PLGA/β-TCP scaffolds were then formed by photocuring with a 405 nm light source. To fabricate the CCL2/GelMA hydrogel/PLGA/β-TCP composite scaffold, 1 μg of CCL2 (cat. no.10134-H08Y; Sino Biological Inc, China) was pre-mixed with the 10% GelMA hydrogel and sonicated until completely dissolved and bubble-free. The resulting scaffolds were categorized into three groups based on their composition: PLGA/β-TCP (PT), GelMA/PLGA/β-TCP (GPT), and CCL2-conjugated GelMA/PLGA/β-TCP (CGPT).

Morphological Observations and Porosity Measurement in Composite Porous Scaffolds

Composite scaffolds with dimensions of 5 × 5 × 5 mm were examined through a scanning electron microscope (SEM) (Zeiss EVO18; Carl Zeiss SMT, Germany). Images were captured at various magnifications (70×, 600×, and 1000×). Localized small particles of the CCL2 sample within the hydrogel composite scaffold were visible. The porosity of each scaffold group was determined using the wetting liquid replacement technique [33].

Sustained Release Measurement Curve of CCL2

In this study, three different concentrations of CCL2/10% GelMA hydrogel mixtures (600, 800, and 1200 pg/mL) were created using the previously described method. Equal volumes of these mixtures were then placed into a 96-well plate to undergo a photocuring process. A specific volume of phosphate buffer saline (PBS) buffer was introduced into each well containing the mixture. Solutions were collected and measured for CCL2 at various time points (2, 3, 5, 7, 10, 14, 21, and 30 d) using the Elisa Kit (MCP-1 Human Instant ELISA Kit; Thermo Fisher Scientific, USA).

Cell Model Experiment of CCL2

Flow Cytometric Analysis for Phenotypic Identification of BMSCs

BMSCs were obtained and grown from three-week-old Sprague-Dawley (SD) rats using a whole-bone marrow technique. The BMSCs were screened for mycoplasma contamination using the Myco-Lumi™ Luminescent Mycoplasma Detection Kit (cat. no.C0298S; Beyotime Institute of Biotechnology), and all tested samples were found to be negative. Once BMSCs reached 80–90% confluence, they were treated with trypsin, neutralized with a complete medium, and their viability was evaluated using Trypan Blue, showing over 90% viability. A cell suspension of 5×10^4 per tube was incubated with FITC Mouse lgG2a, κ Isotype Control Antibody (cat. no. 400207; BioLegend, San Diego, CA, USA), FITC-labeled CD44H (cat. no. 156007; BioLegend, San Diego, CA, USA) and CD90 (cat. no.166403; BioLegend, San Diego, CA, USA), and PE-labeled CD11b/c (cat. no. 201807; BioLegend, San Diego, CA, USA) for 30 min in the dark. Then, the cells were washed with PBS and analyzed using flow cytometry (BD FACSCalibur).

CCK-8 Experiments

The third generation of BMSCs, once digested, was uniformly distributed across a 96-well plate at a density of 2×10^3 cells per well. Following a 24-h incubation with complete culture medium, the medium was removed, and a mixture containing varying concentrations of CCL2, specifically 0, 50, 100, 150, and 200 ng/ml, was added once at the beginning of the experiment. Each concentration group included five replicate wells. After co-culturing for intervals of 24, 48, 72, and 96 h, 10 μL of CCK-8 solution (cat. no. C0038; Beyotime Institute of Biotechnology, China) was added to each well. The absorbance at 450 nm was then recorded using a microplate reader.

Osteogenic Differentiation

Third-generation BMSCs were harvested and seeded in 6-well plates at a density of 2×10^4 cells per cm^2. The cells were cultured in complete DMEM medium, supplemented with 10% fetal bovine serum (FBS) (Gibco, Thermo Fisher Scientific, Inc., USA) and 1% penicillin-streptomycin (Beijing Solarbio Science & Technology Co., Ltd., China), and maintained until they reached 60–70% confluence. The cells were then allocated into four groups based on CCL2 concentrations (0, 100, 200, and 300 ng/mL), with each group having three wells. Following fixation with 4% paraformaldehyde for 30 min and subsequent washing with PBS, calcium nodules were stained with 0.1% alizarin red solution (cat. no. C0148S; Beyotime Institute of Biotechnology, China) at a volume of 1 mL per well for 15 min and subsequently examined and imaged under a microscope (OLYMPUS DP71; Olympus Corporation, Japan).

Tube Formation Assay

In vitro angiogenesis was assessed using a tube formation assay in 24-well plates. Lynjune matrix gel was thawed on ice, and 20 μL was gently dispensed into the center of each well. Using a pre-chilled pipette tip, the gel was evenly spread into a thin layer, carefully avoiding contact with the well walls to minimize material loss and ensure unobstructed imaging fields. Sterile water was added to the inter-well spaces to reduce evaporation. After overnight incubation at 4 °C to allow uniform diffusion, the plates were transferred to 37 °C for complete polymerization. Cells were treated with 0, 100, or 200 ng/mL CCL2, or with 200 ng/mL CCL2 in combination with a CCR2 antagonist (RS504393; Aladdin, China). HUVECs were then seeded at an optimized density of 1.5×10^5 cells per well in 500 μL of complete medium (final concentration: 3×10^5 cells/mL). Tube formation was monitored and imaged 6 h after seeding. These optimized conditions consistently yielded well-defined and robust vascular-like networks.

Animal Experiments

Grouping and Operation of Animals

All animal experiments were carried out under the approval of the Animal Ethics Committee of Guangdong Medical University. **Supplementary Fig. 1** illustrates the methodology employed to create a bone defect model in SD rats. Male rats, each weighing between 350 and 400 grams, underwent osteotomy at the mid-shaft of the left femur. These rats were randomly assigned to one of four groups according to the implant type with eight rats per group: control, PT, GPT, and CGPT. The control group consisted of untreated bone defects without any scaffold implantation. Prior to surgery, the rats were fasted for 8 h and allowed to drink for 2 h. Anesthesia was induced via an intraperitoneal injection of 30 mg/kg of 1% pentobarbital sodium, while monitoring vital signs, such as heart rate and respiration, for indications of a marked decrease in muscle tension and loss of corneal and light reflexes. After disinfecting the left leg's skin with povidone-iodine (PVP-I) twice, the rat was positioned prone. A 1.5-cm incision was made on the lateral side of the left femur, and the superficial fascia, deep fascia, and muscle layers were meticulously separated to reveal the femur. An external fixator (Tianjin Jinlei Technology Co., Ltd.) was used to drill holes at specified locations, followed by the insertion of four screws (4.5 cm in length; 0.7 mm in diameter). The fixator was then secured with clamps and nuts. A 3-mm osteotomy was executed between the second and third screws using a wire saw. After adjusting the external fixator to ensure optimal bone-implant contact at the defect site, the wound was thoroughly irrigated with sterile saline and closed surgically. To prevent postoperative infections, intramuscular penicillin sodium (80,000 IU/kg/day; Harbin Pharmaceutical Group) was administered every 24 h, along with daily monitoring of the wound and application of PVP-I every 24 to 48 h.

Changes in Bone Mass

After 4 or 8 weeks of implantation, micro-CT scanning (SkyScan 1176; Bruker, Germany) was employed to examine the femoral defect sites filled by the composite scaffolds as well as both ends measuring 5 mm at both the top and bottom. The analysis and reconstruction of bone parameters, including BV/TV and BMD, were conducted using NRecon, CTAn, and CTvox software.

Histological Staining and Immunohistochemical Analysis

Following the micro-CT analysis, femur tissue samples were immersed in a 10% EDTA decalcification solution (cat. no. 6381-92-6; Beijing Solarbio Science & Technology Co., Ltd., China) for decalcification, for which the solution was refreshed bi-weekly. After 6 to 8 weeks, successful decalcification was indicated when the bone samples could be easily penetrated by a needle, at which point programmed gradient dehydration was initiated. The specimen was extracted, preserving the area filled with the composite scaffold, as well as a 1-cm segment from both the proximal and distal ends of the bone. An incision was made along the femur's longitudinal axis (sagittal plane), followed by wax immersion and embedding. The embedded samples were then sliced to a thickness of 5 μm using a paraffin slicer (LEICA2155; Leica, Germany) in accordance with experimental protocols. The resulting sections underwent standard processing and were stained with hematoxylin (cat. no. H3136; Sigma-Aldrich) and eosin (cat. no. 318906; Sigma-Aldrich, St. Louis, MO, USA) to detect newly formed bone within the samples. Immunohistochemical analysis was conducted as previously outlined. After decalcification and a gradual hydration process using xylene, the tissue sections were subjected to antigen retrieval and blocking. They were then incubated overnight with primary antibodies diluted to 1:500, including VEGF (cat. no.sc-57496; Santa Cruz Biotechnology, Inc.) and osteogenic transcription factors, such as Runx2 (cat. no. sc-390351; Santa Cruz Biotechnology, Inc.), OPN (cat. no. sc-21742; Santa Cruz Biotechnology, Inc.), and OCN (cat. no. sc-365797; Santa Cruz Biotechnology, Inc.). Following a 24-h incubation with the primary antibodies, the sections were treated with secondary antibodies. The final steps involved dehydrating, clearing, and sealing the sections with neutral resin.

Statistical Methods

All numerical data were organized into statistical tables and presented as mean ± standard deviation (SD). Data were analyzed using SPSS version 20.0 (IBM Corp., Armonk, NY, USA). After checking of normal distribution by Kolmogorov-Smirnov test, all parameters were analyzed by ANOVA and post-hoc Tukey's HSD. Significance levels included $^{*}p < 0.05$, $^{**}p < 0.01$, and $^{***}p < 0.001$, reflecting the presence of statistical differences in the data. The graphical representation was created using GraphPad Prism ver-

sion 8.01 (IBM Corp., Armonk, NY, USA). All *in vitro* experiments were conducted with three biological replicates (n = 3), while the *in vivo* bone defect model included four animals per group (n = 4). Immunohistochemical analyses were quantified using five representative images (n = 5).

Results

Physical Properties and CCL2 Release Profiles of Composite Scaffolds

The composite scaffolds were created as uniform macroporous cubes with dimensions of 5 × 5 × 5 mm^3. Scanning electron microscopy (SEM) was utilized to capture images of these scaffolds at different magnification levels (Fig. 1**A**). At a 70× magnification, all scaffolds displayed macroporous structures without notable variations. The average sizes of the macropores in the PT, GPT, and CGPT groups were around 530, 500, and 540 μm, respectively. The SEM images of the PT group at magnifications of 600× and 1000× revealed a network of small pores interlinked with the larger openings. Conversely, the GPT and CGPT groups at the same magnifications showed a prominent presence of hydrogel filling. Furthermore, the SEM images of the CGPT group illustrated a well-distributed granular material from CCL2 that effectively covered the scaffold's surface. To assess the release profile of CCL2 from GelMA hydrogel under load, a drug release curve was plotted over a span of 30 days. As depicted in Fig. 1**B**, CCL2 exhibited a gradual, time-dependent release during the initial 14 days, with a sharp increase in the first five days followed by a steady rise until it reached its maximum on the 14th day. The concentrations of CCL2 recorded for the low, medium, and high dose groups were 378.9, 544.4, and 850.9 pg/mL, respectively, with cumulative release percentages of 63%, 65.6%, and 71%. Based on the release curves, it can be calculated that a composite scaffold loaded with 1 μg of CCL2 would produce a cumulative peak release of 665.3 ng (Fig. 1**C**). After 14 days, the CCL2 concentration in PBS gradually declined, which may be attributed to the inherent chemical instability of CCL2 in PBS [34]. These findings suggest that GelMA hydrogel possesses remarkable loading capacity and sustained-release characteristics.

Effects of CCL2 on BMSCs Proliferation, Osteogenic ifferentiation and HUVECs Tube Formation

At passage 3, cultured BMSCs displayed a distinct elongated spindle shape with a tightly organized, whorl-like structure (Fig. 2**A**). Flow cytometry confirmed the classic immunophenotype of BMSCs, showing high expression of CD44H (86.3%) and CD90 (96.8%), with minimal expression of CD11b/c (1.2%) (Fig. 2**B**). CCK-8 assays conducted on BMSCs over days 1 to 4 with varying concentrations of CCL2 (0-250 ng/mL) indicated a proliferation increase that was both dose- and time-dependent (Fig. 2**C**). Importantly, the highest concentration of 250 ng/mL CCL2 significantly improved cell viability compared to the control group at all measured time points. Moreover, CCK-8 assays results confirmed that the composite scaffolds of GPT and CGPT did not exert any appreciable inhibitory effects on BMSC viability (Fig. 2**D**). To assess the impact of CCL2 on the mineralization of BMSCs, cells were subjected to osteogenic induction for 21 days with CCL2 (0–300 ng/mL). As illustrated in Fig. 2**E**, the control group showed minimal calcium nodule formation, while the groups treated with CCL2 exhibited central cell clustering, greater calcium accumulation, and a higher number of nodules, suggesting a dose-dependent enhancement of mineralized nodule development in BMSCs. To further examine the functional effects of CCL2 on angiogenesis, tube formation assays were performed in HUVECs treated with CCL2 alone or in combination with a CCR2 antagonist. CCL2 markedly promoted tube formation, whereas the addition of the CCR2 antagonist substantially diminished this effect, indicating that CCL2 facilitates angiogenic tube formation (Fig. 2**F–G**).

Micro-CT and Histological Examination Evaluation of Bone Healing Induced by CCL2-doped Composite Scaffolds

Micro-CT imaging and reconstruction assessments were performed on femur specimens at 4 and 8 weeks following surgery in a bone defect model. The 3D images revealed that the extent of femoral bone regeneration at 8 weeks was notably better than at 4 weeks (Fig. 3**A**). Furthermore, intergroup comparisons showed that both BMD and BV/TV at 8 weeks were significantly elevated compared to the 4-week measurements. At the 8-week mark, the CGPT group exhibited superior bone morphology, with remodeling nearing normalcy, while the GPT, PT, and control groups displayed considerable gaps at the fracture sites. Additionally, the CGPT group had higher BMD readings than the GPT, PT, and control groups at both time points, with BV/TV values reflecting a similar pattern (Fig. 3**B** and 3**C**). Histological examination through HE staining indicated the presence of cellular infiltration and blood vessel-associated fibrous tissue with red blood cells in the CGPT group. By the 8-week evaluation, all groups showed improved healing. However, the CGPT group exhibited more pronounced material degradation, increased mineralized tissue, and a more cohesive interface between the material and tissue compared to the control, PT, and GPT groups (Fig. 3**D**).

Immunohistochemical Evaluation of Bone Healing by CCL2-doped Composite Scaffolds

Immunohistochemical analysis of the femoral samples revealed positive expressions of osteocalcin (OCN), osteopontin (OPN), Runx2, and VEGF in the osteogenic areas across all groups (Fig. 4**A–H**). Notably, at both 4 and 8 weeks, the expression levels of these markers were sig-

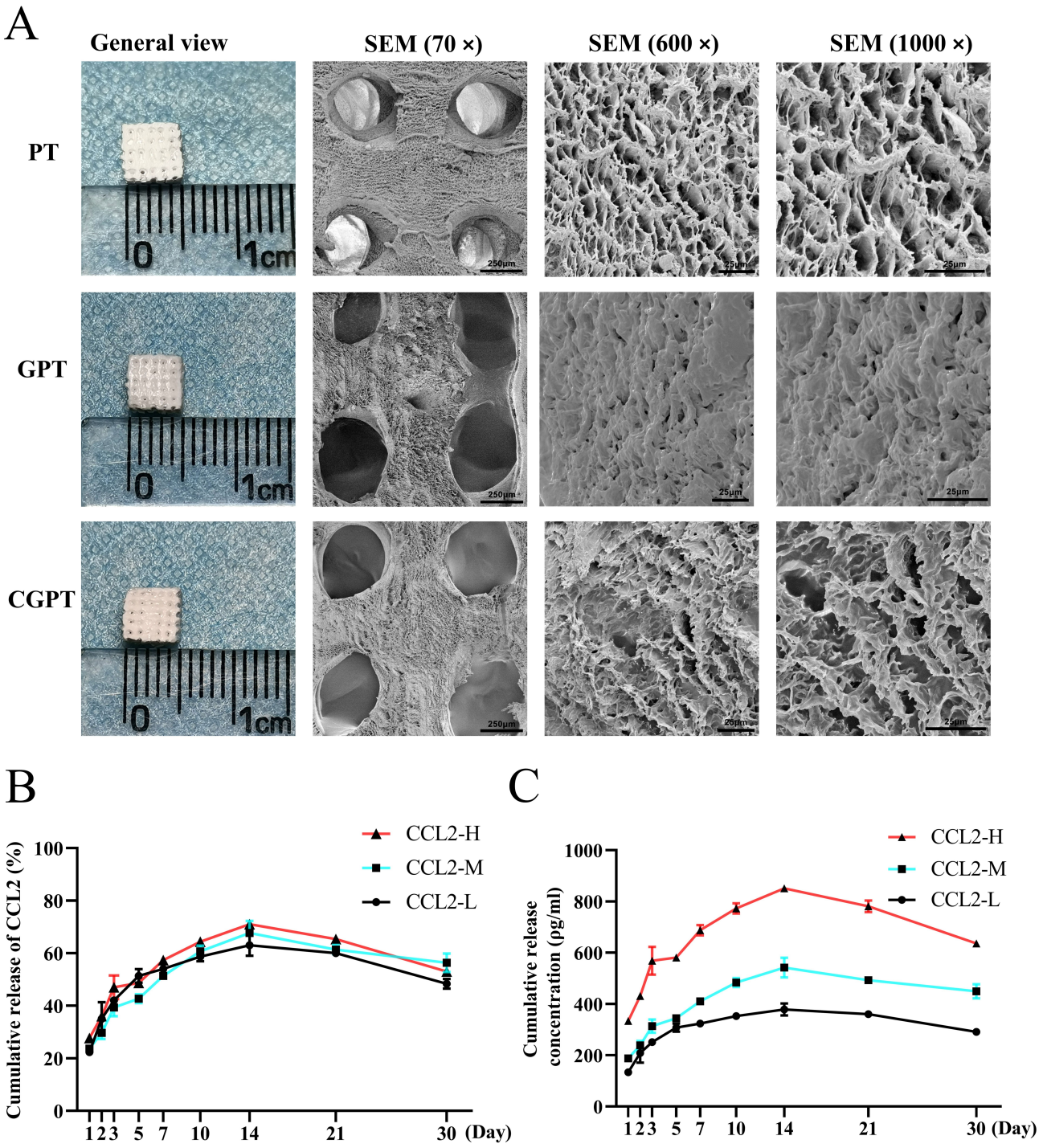

Fig. 1. Characterization and CCL2 release profile of composite scaffolds. (**A**) An in-depth examination of the structural characteristics of composite scaffolds, highlighting the ultrastructural variations and resemblances observed at magnifications of 70×, 600×, and 1000× using SEM. (**B**) Dynamic release profiles of varying CCL2 concentration gradients over a 30-day period, showing cumulative release percentages. (**C**) Dynamic cumulative release concentrations of CCL2 from composite scaffolds with varying concentration gradients over a 30-day period. Scale bar: 250 or 25 μm in A. Data were graphed using GraphPad Prism 8, images were processed in Adobe Photoshop CS6, and final figures were assembled in Microsoft PowerPoint.

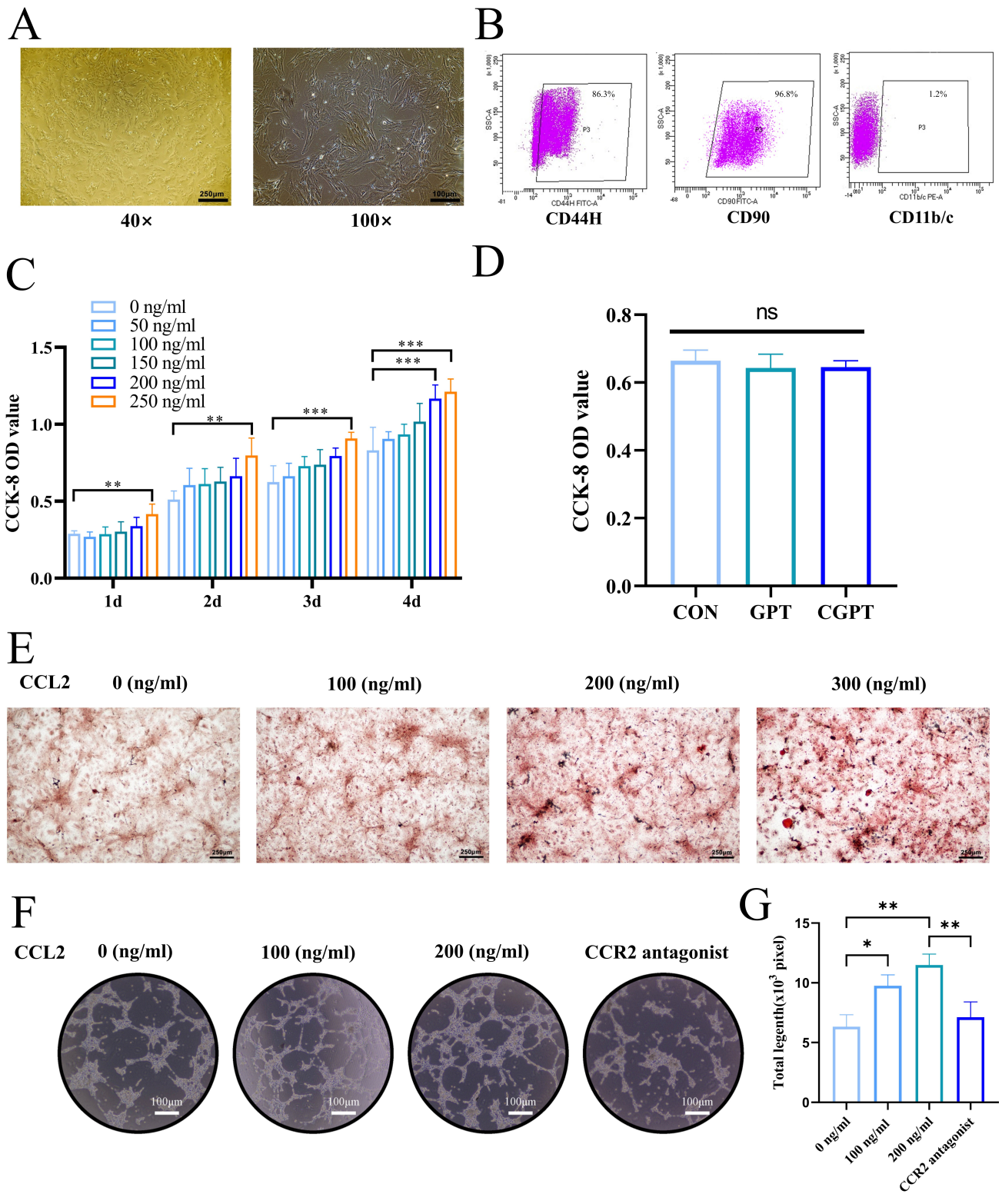

Fig. 2. Effect of CCL2 on proliferation, mineralization and tube formation. (**A**) Microscopic examination of passage 3 BMSCs at 40× and 100× magnification. (**B**) Flow cytometry assessment of protein expression levels for CD44H, CD90, and CD11b/c in BMSCs. (**C**) CCK8 assay to evaluate the impact of varying CCL2 concentrations on BMSC viability over days 1 to 4. (**D**) CCK-8 assay evaluating the effects of GPT and CGPT composite scaffolds on BMSC viability after 48 h. (**E**) Results of Alizarin red staining for BMSCs exposed to different CCL2 concentrations over a 21-day period. (**F**) Tube formation in HUVECs treated with CCL2 or CCL2 plus a CCR2 antagonist. (**G**) Quantitative analysis of total tube length in HUVECs. Data are presented as mean ± SD (n = 3). Statistical significance: $^{*}p < 0.05$, $^{**}p < 0.01$, $^{***}p < 0.001$. Scale bar: 100 or 250 μm in A, E, and F. Data were graphed using GraphPad Prism 8, images were processed in Adobe Photoshop CS6, and final figures were assembled in Microsoft PowerPoint.

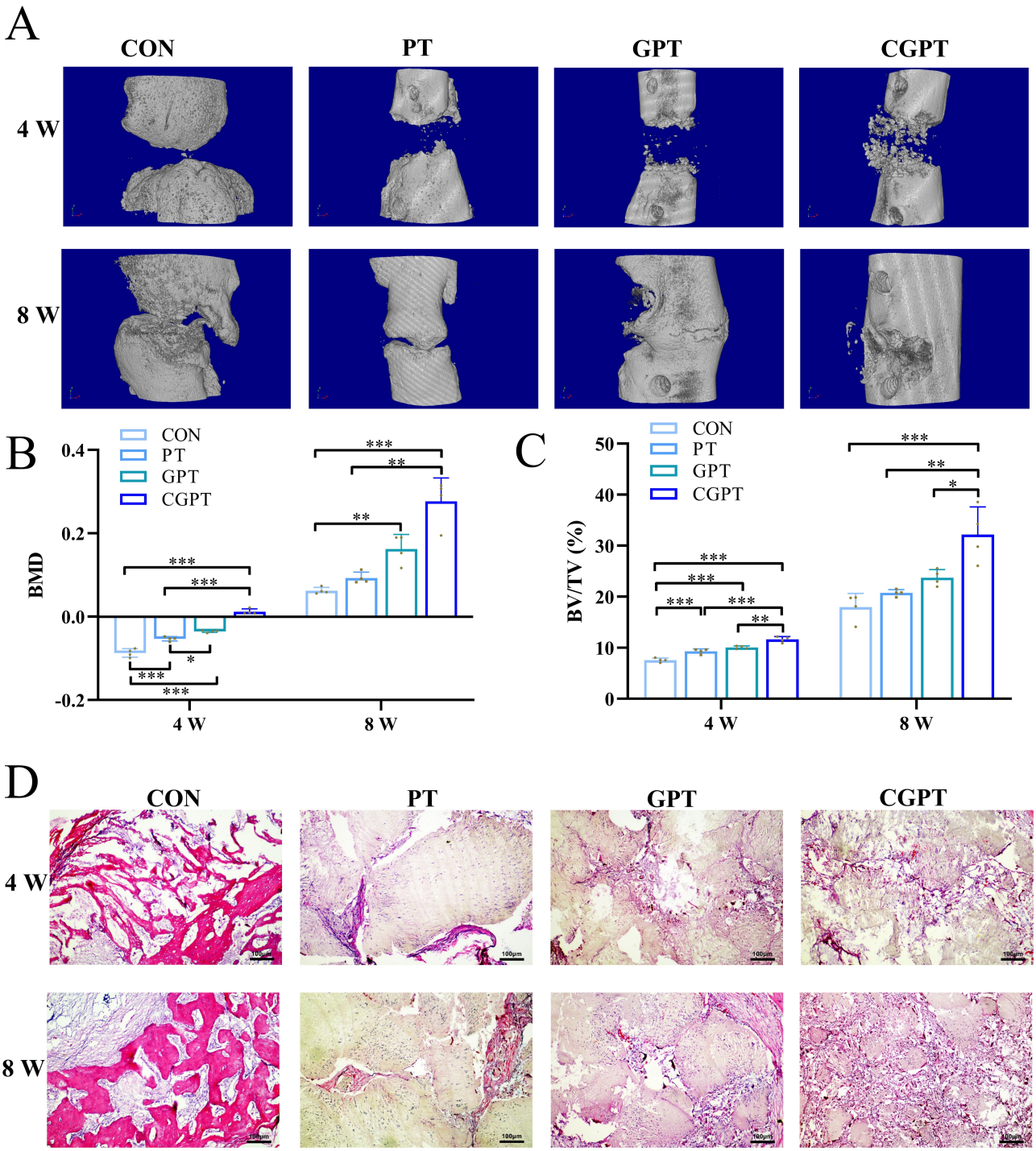

Fig. 3. Bone healing assessed by micro-CT and HE in the CCL2-doped scaffold group. (**A**) Micro-CT assessments illustrate the 3D bone reconstruction BMD and BV/TV for the control, GPT, PT, and CGPT groups at 4 and 8 weeks. (**B**) Quantitative bar graph of BMD. (**C**) Quantitative bar graph of BV/TV (%). (**D**) HE staining outcomes for samples from each group at both 4 and 8 weeks, viewed at 100× magnification. Data are presented as mean ± SD (n = 4). Statistical significance: $^{*}p < 0.05$, $^{**}p < 0.01$, $^{***}p < 0.001$. Scale bar: 100 μm in D. Data were graphed using GraphPad Prism 8, images were processed in Adobe Photoshop CS6, and final figures were assembled in Microsoft PowerPoint.

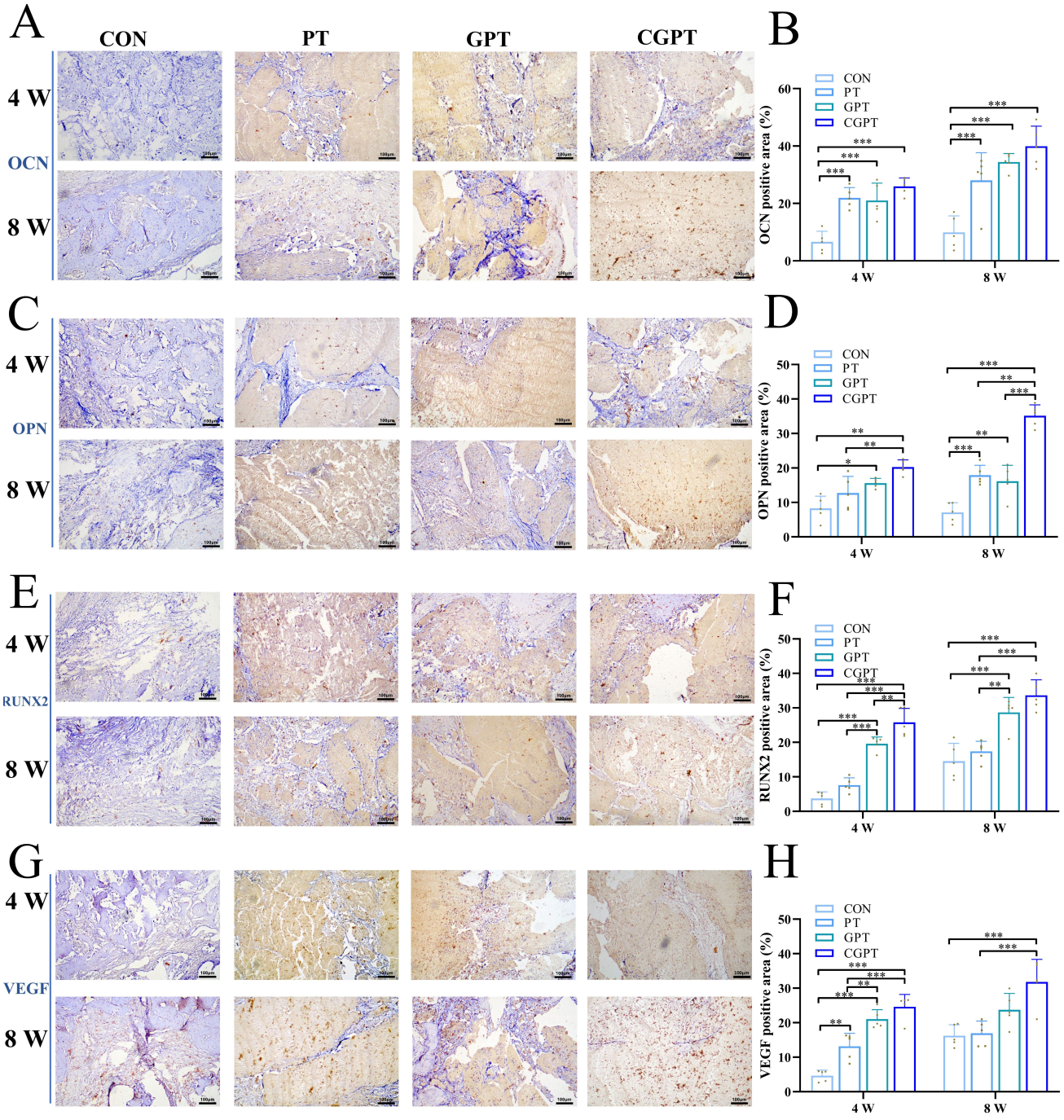

Fig. 4. Immunohistochemical evaluation of bone healing by CCL2-doped composite scaffolds. Representative immunohistochemical staining images and quantitative analysis of osteogenic and angiogenic markers (OCN, OPN, Runx2, and VEGF) in the control, PT, GPT, and CGPT groups at 4 and 8 weeks. (**A**) Immunohistochemical staining of OCN. (**B**) Quantitative analysis of OCN-positive areas. (**C**) Immunohistochemical staining of OPN. (**D**) Quantitative analysis of OPN-positive areas. (**E**) Immunohistochemical staining of Runx2. (**F**) Quantitative analysis of Runx2-positive areas. (**G**) Immunohistochemical staining of VEGF. (**H**) Quantitative analysis of VEGF-positive areas. Data are presented as mean ± SD (n = 5). Statistical significance: $^{*}p < 0.05$, $^{**}p < 0.01$, $^{***}p < 0.001$. Scale bar: 100 μm in A–H. Data were graphed using GraphPad Prism 8, images were processed in Adobe Photoshop CS6, and final figures were assembled in Microsoft PowerPoint.

nificantly elevated in the CGPT group relative to the control, PT, and GPT groups. Moreover, the improvements in these markers at 8 weeks post-surgery were significantly more pronounced than those at 4 weeks, indicating that the CCL2-loaded composite scaffold is highly effective in enhancing osteogenic differentiation and promoting angiogenesis.

Discussion

In bone tissue engineering, composite scaffolds are favored for their physical and chemical properties that support cell adhesion, migration, differentiation, and nutrient-waste exchange [35]. Natural bone is primarily made up of a matrix of hydroxyapatite and collagen fibers [36]. PLGA is widely used for drug and biomolecule delivery due to its capacity to encapsulate both hydrophilic and hydrophobic compounds [37]. Hydrogels offer stimuli-responsive properties (e.g., temperature, pH, light, and biochemical cues), promoting cell growth and uniform nutrient/metabolite transport [38]. Compared with conventional polymer/bioceramic composites, hydrogel-mediated protein delivery provides uniform, sustained factor release, and simpler handling. Incorporating β-TCP enhances mechanical strength and mimics natural bone, offsetting polymer stiffness [28]. A degradable GelMA/PLGA/β-TCP composite scaffold integrates these advantages: β-TCP and PLGA provide osteoconductivity, osteoinductivity, and tunable degradation that aligns with new bone formation, while the GelMA hydrogel offers a porous, bone-mimicking microarchitecture that supports cell adhesion, proliferation, and osteogenic differentiation [39,40]. Compared with single-polymer or ceramic scaffolds, this composite facilitates more efficient bone regeneration and enhanced scaffold–host integration [41–43]. The dimensions of pore size and overall porosity are critical factors influencing osteogenesis; an appropriate pore size can improve capillary and blood vessel formation, which is essential for bone development [44]. It is generally advised that composite scaffolds maintain a porosity between 60% and 90% and an average pore size exceeding 150 μm [45]. Research indicates that lower porosity can enhance mechanical strength and reduce tissue stress, while a decreased level of stimulation may promote osteoblast differentiation [44]. The composite scaffolds examined in this research exhibited an average pore size greater than 500 μm and a porosity exceeding 60%.

CCL2 recruits CCR2 positive monocytes and macrophages to bone injury sites and enhances osteogenesis in MSC macrophage co-cultures. It promotes M2 polarization, increasing IL-10 and reducing pro-inflammatory cytokines such as TNF-α and IL-6. It also enhances angiogenesis through endothelial migration and proliferation, activating the PI3K/Akt, MAPK/ERK, and Wnt/β-catenin pathways, likely underpinning the improved osteogenesis and vascularization observed [18,46–48]. Our findings demonstrated a consistent release pattern of CCL2, with similar release profiles across various concentrations (low, medium, and high), peaking on day 14 with approximately 63–71% of CCL2 released. This release pattern served as a benchmark for subsequent *in vivo* studies in rats. When assessing the impact of CCL2 on BMSCs, CCL2 was found to significantly enhance cell viability compared to lower concentrations at a concentration of 250 ng/ml, indicating a dose-dependent effect with heightened cell proliferation at higher levels. BMSCs were exposed to different concentrations of CCL2 to stimulate osteogenic differentiation, and Alizarin red staining demonstrated an increase in calcium nodule formation correlating with elevated CCL2 levels, confirming the dose-dependent enhancement of BMSC mineralization. Furthermore, tube formation assays showed that CCL2 promoted angiogenic tube formation in HUVECs, whereas co-treatment with a CCR2 antagonist significantly reduced this effect, supporting the pro-angiogenic function of CCL2.

Bioactive agents that facilitate controlled and sustained release, or cells, are incorporated into composite scaffolds to enhance cell proliferation and differentiation, and have found extensive applications in bone tissue engineering[49,50]. For instance, BMP-2 is known to trigger osteogenic responses and promote bone formation, establishing itself as a key factor in the differentiation of bone marrow mesenchymal stem cells [51]. In another approach, osteoblasts and chondrocytes were simultaneously cultured and implanted into a TCP scaffold, resulting in a dual-layer composite scaffold that encouraged the development of osteochondrocytes [52]. Recent studies highlight muscle-bone biochemical cross-talk as a key regulator of musculoskeletal homeostasis [53]. Bone-derived osteocalcin promotes osteoblast differentiation and enhances muscle function, while muscle-derived myokines modulate bone remodeling; for example, irisin stimulates bone formation, whereas myostatin inhibits both muscle and bone growth [54]. In composite biodegradable scaffolds, osteocalcin may thus support local bone regeneration while influencing systemic musculoskeletal dynamics, underscoring the potential for scaffold design to integrate bone repair with broader musculoskeletal regulation [55,56]. Micro-CT 3D imaging of femoral specimens indicated that the composite scaffold loaded with CCL2 significantly improved bone regeneration when compared to both control and non-CCL2 groups. The CCL2 scaffold demonstrated enhanced bone formation and a more developed bone structure, with remodeling patterns closely resembling those of healthy bone. These findings were corroborated by quantitative bone assessments, which indicated elevated BV/TV and BMD metrics in the presence of CCL2. Histological analysis further revealed a more cohesive interface between the scaffold and tissue, characterized by a less distinct boundary, and an enlarged mineralized region. Immunohistochemical staining

highlighted a stronger expression of osteogenic and angiogenic markers (OCN, OPN, Runx2, and VEGF) at the interface of the CCL2 composite scaffold.

Our findings indicate that CCL2 contributes to osteogenic repair; however, we did not compare its effects with other bone inducers such as BMP-2, the only FDA-approved osteogenic protein, and biomechanical testing was not performed due to the early sampling time and limited mechanical integrity of newly formed tissue. While micro-CT and histological analyses demonstrated enhanced osteogenesis and angiogenesis, these results reflect structural and biological improvements rather than confirmed functional recovery, as mechanical competence cannot be inferred solely from morphology or protein expression. Furthermore, our evaluation of angiogenesis was limited by the absence of immunofluorescence staining for endothelial and vascular maturation markers such as CD31 and α-SMA, which would enable direct visualization and quantification of neovascularization. Although VEGF immunohistochemistry and supplementary *in-vitro* assays offer supportive evidence, the lack of these *in-vivo* angiogenic markers remains a notable limitation that warrants further investigation. To address these limitations, future studies should include BMP-2 as a positive control to more comprehensively assess the osteogenic potential of CCL2-loaded scaffolds, perform biomechanical testing at later time points to confirm functional recovery, and incorporate additional *in-vivo* angiogenesis markers such as CD31 and α-SMA for quantitative evaluation.

Importantly, high doses of CCL2 may pose potential safety risks, including local or systemic tumorigenic effects, chronic inflammation, and fibrotic tissue formation[57,58]. Since our current study did not include hematology, serum chemistry, or histological evaluation of distant organs, a comprehensive safety profile cannot yet be established. Future studies should aim to define the minimum effective dose and establish a safe dose ceiling, incorporating longitudinal monitoring of systemic biomarkers and detailed histopathological assessments. Furthermore, translational validation in large-animal models will be critical, employing sustained-release scaffolds, multiple dose levels, and long-term assessment of mechanical competence, alongside functional, imaging, and vascular analyses. Direct comparisons with BMP-2 will also help contextualize the osteogenic potential of CCL2 and inform translations into clinical practice. Additionally, *in vitro* and *in vivo* studies using CCR2 antagonists or anti-CCL2 neutralizing antibodies are essential to definitively establish the causal role of CCL2-CCR2 signaling.

Conclusions

This study demonstrated that CCL2-doped GelMA/PLGA/β-TCP composite scaffolds significantly enhance bone regeneration through dual osteogenic and angiogenic mechanisms. Compared with previous CCL2-based strategies, our scaffold achieves sustained, localized release of CCL2 while synergizing with the 3D-printed composite microenvironment, promoting BMSC proliferation and mineralization *in vitro* and accelerating *in vivo* bone defect healing. This is evidenced by increased bone mass (BMD and BV/TV), elevated osteogenic markers (Runx2, OPN, and OCN), and enhanced vascularization (VEGF). These findings highlight a novel mechanistic and translational advance beyond simple "factor swapping", offering a promising alternative to conventional bone grafts.

List of Abbreviations

β-TCP, β-tricalcium phosphate; BMD, bone mineral density; BMP2, bone morphogenetic protein; BMSCs, bone marrow mesenchymal stem cells; BV/TV, bone volume fraction; CCL2, Chemokine (C-C motif) ligand 2; CGPT, CCL2-embedded GelMA/PLGA/β-TCP; GelMA, gelatin methacrylate; GPT, GelMA/PLGA/β-TCP; MCP1, monocyte chemokine 1; MSC, mesenchymal stem cells; OPN, osteopontin; OCN, osteocalcin; PLGA, polylactic acid-glycolic acid; PT, PLGA/β-TCP; PTH, parathyroid hormone; Runx2, Runt-related transcription factor 2; VEGF, vascular endothelial growth factor.

AI Application Statement

Artificial intelligence–assisted tools were used exclusively for language editing to enhance clarity and grammar of the manuscript. The authors retain full responsibility for the integrity of the work, including the accuracy of the data, analyses, and conclusions presented.

Availability of Data and Materials

The datasets used and/or analyzed during the current study are available from the corresponding authors on reasonable request.

Author Contributions

ZL and XP contributed to the design of this work. HNY and BX contributed to the interpretation of data. ZPS, HP, and CSH analyzed the data. ZL and HP drafted the work. BW and SEL revised critically for important intellectual content. All authors read and approved the final manuscript. All authors agree to be accountable for all aspects of the work in ensuring that questions related to the accuracy or integrity of any part of the work are appropriately investigated and resolved. All authors read and approved the final manuscript.

Ethics Approval and Consent to Participate

This study involving animal experiments was approved by the Ethics Committee of Guangdong Medical University (Approval ID: GDY1902126; Date: May 25, 2019).

Acknowledgments

The authors gratefully acknowledge BioRender.com for providing the platform used to create the schematic figures in this study. We thank Mr. Xinyuan Wu for creating the graphical abstract and Mr. Dongping Li for his assistance in obtaining the publication license.

Funding

This work was supported by: Guangdong Medical Science and Technology Research Fund Project (B2024006); Research Project of Guangdong Provincial Bureau of Traditional Chinese Medicine (20251205, 20261199); Guangdong Higher Education Association's "14th Five Year Plan" 2024 Higher Education Research Project (24GQN06); Zhanjiang Science and Technology Development Special Fund (2022A01176, 2025A502026, 2025A502021); Guangdong Medical University Affiliated Hospital High-level Talent Research Launch Project (GCC2022008, GCC2024022); Affiliated Hospital of Guangdong Medical University Clinical Research Program(LCYJ2019B012); National Natural Science Foundation of China (82272505, 82472454, 81874000); Natural Science Foundation of Guangdong Province (2023A1515011040); Research Grants Council of Hong Kong (14119124, 14113723, 14121721, N_CUHK472/22, T13-402/17-N, AoE/M-402/20); Special Project for Clinical and Basic Sci & Tech Innovation of Guangdong Medical University(GDMULCJC2025049, GDMULCJC2025063). Funders had no role in study design, data collection/analysis, or manuscript preparation.

Conflict of Interest

The authors declare no conflict of interest.

Supplementary Material

Supplementary material associated with this article can be found, in the online version, at https://doi.org/10.22203/eCM.v057a08.

References

[1] Wildemann B, Ignatius A, Leung F, Taitsman LA, Smith RM, Pesántez R, *et al*. Non-union bone fractures. Nature Reviews. Disease Primers. 2021; 7: 57. https://doi.org/10.1038/s41572-021-00289-8.

[2] Bowers KM, Anderson DE. Delayed Union and Nonunion: Current Concepts, Prevention, and Correction: A Review. Bioengineering. 2024; 11: 525. https://doi.org/10.3390/bioengineering11060525.

[3] Gómez-Barrena E, Ehrnthaller C. Long bone uninfected non-union: grafting techniques. EFORT Open Reviews. 2024; 9: 329–338. https://doi.org/10.1530/EOR-24-0032.

[4] Alford AI, Nicolaou D, Hake M, McBride-Gagyi S. Masquelet's induced membrane technique: Review of current concepts and future directions. Journal of Orthopaedic Research: Official Publication of the Orthopaedic Research Society. 2021; 39: 707–718. https://doi.org/10.1002/jor.24978.

[5] Battafarano G, Rossi M, De Martino V, Marampon F, Borro L, Secinaro A, *et al*. Strategies for Bone Regeneration: From Graft to Tissue Engineering. International Journal of Molecular Sciences. 2021; 22: 1128. https://doi.org/10.3390/ijms22031128.

[6] Graham SM, Leonidou A, Aslam-Pervez N, Hamza A, Panteliadis P, Heliotis M, *et al*. Biological therapy of bone defects: the immunology of bone allo-transplantation. Expert Opinion on Biological Therapy. 2010; 10: 885–901. https://doi.org/10.1517/14712598.2010.481669.

[7] Schmidt AH. Autologous bone graft: Is it still the gold standard? Injury. 2021; 52 Suppl 2: S18–S22. https://doi.org/10.1016/j.injury.2021.01.043.

[8] Ahmed N, Eras V, Pruß A, Perka C, Brune J, Vu-Han TL. Allografts: expanding the surgeon's armamentarium. Cell and Tissue Banking. 2023; 24: 273–283. https://doi.org/10.1007/s10561-022-10015-7.

[9] Zhu S, Liu M, Bennett S, Wang Z, Pfleger KDG, Xu J. The molecular structure and role of CCL2 (MCP-1) and C-C chemokine receptor CCR2 in skeletal biology and diseases. Journal of Cellular Physiology. 2021; 236: 7211–7222. https://doi.org/10.1002/jcp.30375.

[10] Toya M, Zhang N, Tsubosaka M, Kushioka J, Gao Q, Li X, *et al*. CCL2 promotes osteogenesis by facilitating macrophage migration during acute inflammation. Frontiers in Cell and Developmental Biology. 2023; 11: 1213641. https://doi.org/10.3389/fcell.2023.1213641.

[11] Wang YF, Yu L, Hu ZL, Fang YF, Shen YY, Song MF, *et al*. Regulation of CCL2 by EZH2 affects tumor-associated macrophages polarization and infiltration in breast cancer. Cell Death & Disease. 2022; 13: 748. https://doi.org/10.1038/s41419-022-05169-x.

[12] Whelan DS, Caplice NM, Clover AJP. Mesenchymal stromal cell derived CCL2 is required for accelerated wound healing. Scientific Reports. 2020; 10: 2642. https://doi.org/10.1038/s41598-020-59174-1.

[13] Jablonski CL, Leonard C, Salo P, Krawetz RJ. CCL2 But Not CCR2 Is Required for Spontaneous Articular Cartilage Regeneration Post-Injury. Journal of Orthopaedic Research: Official Publication of the Orthopaedic Research Society. 2019; 37: 2561–2574. https://doi.org/10.1002/jor.24444.

[14] Fang B, Wang X, Sun Y, Xiong X, Meng X, Li W, *et al*. Hypoxia-induced CCL2/CCR2 axis in adipose-derived stem cells (ADSCs) promotes angiogenesis by human dermal microvascular endothelial cells (HDMECs) in flap tissues. Journal of Physiology and Biochemistry. 2023; 79: 327–339. https://doi.org/10.1007/s13105-023-00944-6.

[15] Xu M, Wang Y, Xia R, Wei Y, Wei X. Role of the CCL2-CCR2 signalling axis in cancer: Mechanisms and therapeutic targeting. Cell Proliferation. 2021; 54: e13115. https://doi.org/10.1111/cpr.13115.

[16] Peng Z, Pang H, Wu H, Peng X, Tan Q, Lin S, *et al*. CCL2 promotes proliferation, migration and angiogenesis through the MAPK/ERK1/2/MMP9, PI3K/AKT, Wnt/β-catenin signaling pathways in HUVECs. Experimental and Therapeutic Medicine. 2022; 25: 77. https://doi.org/10.3892/etm.2022.11776.

[17] Thomann S, Weiler SME, Wei T, Sticht C, De La Torre C, Tóth M, *et al*. YAP-induced Ccl2 expression is associated with a switch in hepatic macrophage identity and vascular remodelling in liver cancer. Liver International: Official Journal of the International Association for the Study of the Liver. 2021; 41: 3011–3023. https://doi.org/10.1111/liv.15048.

[18] Pan D, Acevedo-Cintrón JA, Sayanagi J, Snyder-Warwick AK, Mackinnon SE, Wood MD. The CCL2/CCR2 axis is critical to recruiting macrophages into acellular nerve allograft bridging a nerve gap to promote angiogenesis and regeneration. Experimental Neurology. 2020; 331: 113363. https://doi.org/10.1016/j.expneurol.2020.113363.

[19] Hu Y, Wang L, Zhao Z, Lu W, Fan J, Gao B, *et al*. Cytokines CCL2 and CXCL1 may be potential novel predictors of early bone loss. Molecular Medicine Reports. 2020; 22: 4716–4724. https://doi.org/10.3892/mmr.2020.11543.

[20] Guo Q, Liu Z, Wang M, Guo S, Cong H, Liu L. Analysis on the ex-

pression and value of CCL2 and CCL3 in patients with osteoarthritis. Experimental and Molecular Pathology. 2021; 118: 104576. https://doi.org/10.1016/j.yexmp.2020.104576.

[21] Yao Z, Chen P, Fan L, Chen P, Zhang X, Yu B. CCL2 is a critical mechano-responsive mediator in crosstalk between osteoblasts and bone mesenchymal stromal cells. FASEB Journal: Official Publication of the Federation of American Societies for Experimental Biology. 2021; 35: e21851. https://doi.org/10.1096/fj.202002808RR.

[22] Flegar D, Filipović M, Šućur A, Markotić A, Lukač N, Šisl D, *et al*. Preventive CCL2/CCR2 Axis Blockade Suppresses Osteoclast Activity in a Mouse Model of Rheumatoid Arthritis by Reducing Homing of CCR2(hi) Osteoclast Progenitors to the Affected Bone. Frontiers in Immunology. 2021; 12: 767231. https://doi.org/10.3389/fimmu.2021.767231.

[23] Adekoya TO, Richardson RM. Cytokines and Chemokines as Mediators of Prostate Cancer Metastasis. International Journal of Molecular Sciences. 2020; 21: 4449. https://doi.org/10.3390/ijms21124449.

[24] Gheorghe-Milea A, Stănoiu-Pînzariu O, Georgescu CE. Unravelling the link between chronic inflammation and primary hyperparathyroidism: a systematic review. Frontiers in Immunology. 2025; 16: 1563967. https://doi.org/10.3389/fimmu.2025.1563967.

[25] Vrana NE, Gupta S, Mitra K, Rizvanov AA, Solovyeva VV, Antmen E, *et al*. From 3D printing to 3D bioprinting: the material properties of polymeric material and its derived bioink for achieving tissue specific architectures. Cell and Tissue Banking. 2022; 23: 417–440. https://doi.org/10.1007/s10561-021-09975-z.

[26] Lin H, Zhang L, Zhang Q, Wang Q, Wang X, Yan G. Mechanism and application of 3D-printed degradable bioceramic scaffolds for bone repair. Biomaterials Science. 2023; 11: 7034–7050. https://doi.org/10.1039/d3bm01214j.

[27] Su Y, Zhang B, Sun R, Liu W, Zhu Q, Zhang X, *et al*. PLGA-based biodegradable microspheres in drug delivery: recent advances in research and application. Drug Delivery. 2021; 28: 1397–1418. https://doi.org/10.1080/10717544.2021.1938756.

[28] Bohner M, Santoni BLG, Döbelin N. β-tricalcium phosphate for bone substitution: Synthesis and properties. Acta Biomaterialia. 2020; 113: 23–41. https://doi.org/10.1016/j.actbio.2020.06.022.

[29] Sohier J, Daculsi G, Sourice S, de Groot K, Layrolle P. Porous beta tricalcium phosphate scaffolds used as a BMP-2 delivery system for bone tissue engineering. Journal of Biomedical Materials Research. Part A. 2010; 92: 1105–1114. https://doi.org/10.1002/jbm.a.32467.

[30] Yang P, Wang C, Shi Z, Huang X, Dang X, Li X, *et al*. rhVEGF165 delivered in a porous beta-tricalcium phosphate scaffold accelerates bridging of critical-sized defects in rabbit radii. Journal of Biomedical Materials Research. Part A. 2010; 92: 626–640. https://doi.org/10.1002/jbm.a.32403.

[31] Tan N, Sabalic-Schoener M, Nguyen L, D'Aiuto F. β-Tricalcium Phosphate-Loaded Chitosan-Based Thermosensitive Hydrogel for Periodontal Regeneration. Polymers. 2023; 15: 4146. https://doi.org/10.3390/polym15204146.

[32] Lin S, Cui L, Chen G, Huang J, Yang Y, Zou K, *et al*. PLGA/β-TCP composite scaffold incorporating salvianolic acid B promotes bone fusion by angiogenesis and osteogenesis in a rat spinal fusion model. Biomaterials. 2019; 196: 109–121. https://doi.org/10.1016/j.biomaterials.2018.04.004.

[33] Yang J, Shi G, Bei J, Wang S, Cao Y, Shang Q, *et al*. Fabrication and surface modification of macroporous poly(L-lactic acid) and poly(L-lactic-co-glycolic acid) (70/30) cell scaffolds for human skin fibroblast cell culture. Journal of Biomedical Materials Research. 2002; 62: 438–446. https://doi.org/10.1002/jbm.10318.

[34] Leemasawatdigul K, Gappa-Fahlenkamp H. Effect of storage conditions on the stability of recombinant human MCP-1/CCL2. Biologicals: Journal of the International Association of Biological Standardization. 2011; 39: 29–32. https://doi.org/10.1016/j.biologicals.2010.09.003.

[35] Álvarez-Chimal R, Arenas-Alatorre JÁ, Álvarez-Pérez MA. Nanoparticle-polymer composite scaffolds for bone tissue engineering. A review. European Polymer Journal. 2024; 213: 113093. https://doi.org/10.1016/j.eurpolymj.2024.113093.

[36] Kim C, Lee JW, Heo JH, Park C, Kim DH, Yi GS, *et al*. Natural bone-mimicking nanopore-incorporated hydroxyapatite scaffolds for enhanced bone tissue regeneration. Biomaterials Research. 2022; 26: 7. https://doi.org/10.1186/s40824-022-00253-x.

[37] Hassan M, Abdelnabi HA, Mohsin S. Harnessing the Potential of PLGA Nanoparticles for Enhanced Bone Regeneration. Pharmaceutics. 2024; 16: 273. https://doi.org/10.3390/pharmaceutics16020273.

[38] Cao H, Duan L, Zhang Y, Cao J, Zhang K. Current hydrogel advances in physicochemical and biological response-driven biomedical application diversity. Signal Transduction and Targeted Therapy. 2021; 6: 426. https://doi.org/10.1038/s41392-021-00830-x.

[39] Kang Y, Scully A, Young DA, Kim S, Tsao H, Sen M, *et al*. Enhanced mechanical performance and biological evaluation of a PLGA coated β-TCP composite scaffold for load-bearing applications. European Polymer Journal. 2011; 47: 1569–1577. https://doi.org/10.1016/j.eurpolymj.2011.05.004.

[40] Yue K, Trujillo-de Santiago G, Alvarez MM, Tamayol A, Annabi N, Khademhosseini A. Synthesis, properties, and biomedical applications of gelatin methacryloyl (GelMA) hydrogels. Biomaterials. 2015; 73: 254–271. https://doi.org/10.1016/j.biomaterials.2015.08.045.

[41] Zhang X, Wang X, Lee YW, Feng L, Wang B, Pan Q, *et al*. Bioactive Scaffold Fabricated by 3D Printing for Enhancing Osteoporotic Bone Regeneration. Bioengineering. 2022; 9: 525. https://doi.org/10.3390/bioengineering9100525.

[42] Lao HD, Liu D, Yi R, Yuan YN, Zhao M, Li GS, *et al*. Seawater-contaminated ulnar rabbit bone defects repair using 3D-printed β-TCP/vancomycin composite scaffolds. European Cells & Materials. 2025; 52: 98–113. https://doi.org/10.22203/eCM.v052a07.

[43] Wang W, Zhang B, Li M, Li J, Zhang C, Han Y, *et al*. 3D printing of PLA/n-HA composite scaffolds with customized mechanical properties and biological functions for bone tissue engineering. Composites Part B: Engineering. 2021; 224: 109192. https://doi.org/10.1016/j.compositesb.2021.109192.

[44] Karageorgiou V, Kaplan D. Porosity of 3D biomaterial scaffolds and osteogenesis. Biomaterials. 2005; 26: 5474–5491. https://doi.org/10.1016/j.biomaterials.2005.02.002.

[45] Marew T, Birhanu G. Three dimensional printed nanostructure biomaterials for bone tissue engineering. Regenerative Therapy. 2021; 18: 102–111. https://doi.org/10.1016/j.reth.2021.05.001.

[46] Kasemsuk T, Phuagkhaopong S, Yubolphan R, Rungreangplangkool N, Vivithanaporn P. Cadmium induces CCL2 production in glioblastoma cells via activation of MAPK, PI3K, and PKC pathways. Journal of Immunotoxicology. 2020; 17: 186–193. https://doi.org/10.1080/1547691X.2020.1829211.

[47] Shinohara I, Tsubosaka M, Toya M, Lee ML, Kushioka J, Murayama M, *et al*. C-C Motif Chemokine Ligand 2 Enhances Macrophage Chemotaxis, Osteogenesis, and Angiogenesis during the Inflammatory Phase of Bone Regeneration. Biomolecules. 2023; 13: 1665. https://doi.org/10.3390/biom13111665.

[48] Sierra-Filardi E, Nieto C, Domínguez-Soto A, Barroso R, Sánchez-Mateos P, Puig-Kroger A, *et al*. CCL2 Shapes Macrophage Polarization by GM-CSF and M-CSF: Identification of CCL2/CCR2-Dependent Gene Expression Profile. The Journal of Immunology: Official Journal of the American Association of Immunologists. 2014; 192: 3858–3867. https://doi.org/10.4049/jimmunol.1302821.

[49] Chauhan A, Alam MA, Kaur A, Malviya R. Advancements and Utilizations of Scaffolds in Tissue Engineering and Drug Delivery. Current Drug Targets. 2023; 24: 13–40. https://doi.org/10.2174/1389450123666221011100235.

[50] Vo TN, Kasper FK, Mikos AG. Strategies for controlled delivery of growth factors and cells for bone regeneration. Advanced Drug

Delivery Reviews. 2012; 64: 1292–1309. https://doi.org/10.1016/j.addr.2012.01.016.

[51] Thomas S, Jaganathan BG. Signaling network regulating osteogenesis in mesenchymal stem cells. Journal of Cell Communication and Signaling. 2022; 16: 47–61. https://doi.org/10.1007/s12079-021-00635-1.

[52] Fu R, Liu C, Yan Y, Li Q, Huang RL. Bone defect reconstruction via endochondral ossification: A developmental engineering strategy. Journal of Tissue Engineering. 2021; 12: 20417314211004211. https://doi.org/10.1177/20417314211004211.

[53] Brotto M, Johnson ML. Endocrine crosstalk between muscle and bone. Current Osteoporosis Reports. 2014; 12: 135–141. https://doi.org/10.1007/s11914-014-0209-0.

[54] Shao M, Wang Q, Lv Q, Zhang Y, Gao G, Lu S. Advances in the research on myokine-driven regulation of bone metabolism. Heliyon. 2023; 10: e22547. https://doi.org/10.1016/j.heliyon.2023.e22547.

[55] Mao GZ, Chen YN, Zhao QH. Muscle-bone crosstalk: involvement of myokines in the regulation of osteoporosis. European Cells & Materials. 2024; 48: 115–136. https://doi.org/10.22203/eCM.v048a07.

[56] He T, Qin L, Chen S, Huo S, Li J, Zhang F, *et al*. Bone-derived factors mediate crosstalk between skeletal and extra-skeletal organs. Bone Research. 2025; 13: 49. https://doi.org/10.1038/s41413-025-00424-1.

[57] Singh S, Anshita D, Ravichandiran V. MCP-1: Function, regulation, and involvement in disease. International Immunopharmacology. 2021; 101: 107598. https://doi.org/10.1016/j.intimp.2021.107598.

[58] Jin J, Lin J, Xu A, Lou J, Qian C, Li X, *et al*. CCL2: An Important Mediator Between Tumor Cells and Host Cells in Tumor Microenvironment. Frontiers in Oncology. 2021; 11: 722916. https://doi.org/10.3389/fonc.2021.722916.

Editor's note: The Scientific Editors responsible for this paper were Fergal J. O'Brien and Martin Stoddart.

Received: 27th August 2025; **Accepted**: 25th March 2026; **Published**: 26th June 2026